sustainability

MDPI

Article

Thermal Performance Analysis of Porous Foam-Assisted Flat-Plate Solar Collectors with Nanofluids

Xinwei Lin [1], Yongfang Xia [1,*], Zude Cheng [1], Xianshuang Liu [1], Yingmei Fu [1], Lingyun Li [1] and Wenqin Zhou [2]

1 School of Environment and Energy Engineering, Anhui Jianzhu University, Hefei 230009, China; lxw@stu.ahjzu.edu.cn (X.L.); czd@ahjzu.edu.cn (Z.C.); lxs512@stu.webvpn.ahjzu.edu.cn (X.L.); fym@stu.ahjzu.edu.cn (Y.F.); lilingyun1996@stu.ahjzu.edu.cn (L.L.)

2 School of Electronic and Information Engineering, Anhui Jianzhu University, Hefei 230009, China; 17805622298@163.com

* Correspondence: xiayf@ahjzu.edu.cn

Abstract: This study proposed a model of a porous media-assisted flat-plate solar collector (FPSC) using nanofluid flow. The heightened thermal efficiency of FPSC undergoes numerical scrutiny, incorporating various factors for analysis, including aspects like the configuration of the porous block introduced, Darcy number (Da = 10^{-5}~10^{-2}), types of nanoparticles, volume fraction (φ), and mixing ratio (φ_c). The numerical findings indicate that the dominant factor in the channel is the global Nusselt number (Nu_g). As the Darcy number rises, there is an improvement in the heat transfer performance within the channel. Simultaneously, for the case of Re = 234, φ = 3%, and φ_c = 100%, the Nu_g in the channel reaches a maximum value of 6.80, and the thermal efficiency can be increased to 70.5% with the insertion of rectangular porous blocks of Da = 10^{-2}. Finally, the performance evaluation criteria (PEC) are employed for a comprehensive assessment of the thermal performance of FPSC. This analysis considers both the improved heat transfer and the pressure drop in the collector channel. The FPSC registered a maximum PEC value of 1.8 when rectangular porous blocks were inserted under conditions of Da = 10^{-2} and Re = 234 and the nanofluid concentrations of φ = 3% and φ_c = 100%. The findings can be provided to technically support the future commercial applications of FPSC. The findings may serve as a technical foundation for FPSC in upcoming porous media and support commercial applications.

Keywords: nanofluids; porous material; flat-plate solar collector; thermal performance enhancement; thermal efficiency; performance evaluation criteria

Citation: Lin, X.; Xia, Y.; Cheng, Z.; Liu, X.; Fu, Y.; Li, L.; Zhou, W. Thermal Performance Analysis of Porous Foam-Assisted Flat-Plate Solar Collectors with Nanofluids. *Sustainability* **2024**, *16*, 693. https://doi.org/10.3390/su16020693

Academic Editor: Sergio Nardini

Received: 4 December 2023
Revised: 28 December 2023
Accepted: 8 January 2024
Published: 12 January 2024

1. Introduction

The worldwide energy demand is increasing steadily. This scenario is intensifying the risk of depleting finite fossil fuels and contributing to global warming. Based on the aim of decarbonization, the adjustment of the energy structure has been and is under transition to mitigate climate change [1]. For the developing renewable energy utilization, the flat-plate solar collector (FPSC), a prevalent technology in solar thermal utilization, boasts the benefits of a straightforward structure, low manufacturing and operational costs, and a high level of integration with buildings, as well as a wide range of potential applications [2–4].

Nevertheless, FPSCs mostly have low thermal performance due to more thermal losses and simple heat transfer configurations [5]. To enhance the thermal efficiency of FPSCs, extensive efforts have been devoted to improving their energy efficiency, such as efficient heat transfer structure [5–7], heat pipe technology [8,9], etc. Additionally, porous materials with excellent conductivity and effective energy storage have been incorporated as a highly efficient and cost-effective method to enhance heat transfer and energy efficiency in solar energy systems [10–12]. Moreover, in terms of the working fluid development, nanofluids have also become a promising technique used for enhancing the rate of energy transfer in the FPSC channels [13–15].

Capitalizing on the advantages of porous metal foam for enhancing thermal performance in the FPSC channel, this experimental study unequivocally illustrated that the FPSC channel with completely filled porous media achieves superior thermal efficiency, and even the global Nusselt number experiences an 82% enhancement compared to the empty channel [16]. Moreover, the thermo-physical properties of the porous materials were demonstrated to make a significant impact on the thermal performance of FPSCs [17]. In the majority of numerical studies focusing on improving the thermal performance of FPSCs with porous media assistance, Darcy's law and the Darcy–Brinkman–Forchheimer equation have been primarily used in the porous region [18,19].

In the heat transfer model within the porous region, the assumption of local thermal equilibrium (LTE) is typically applicable in the low-temperature FPSC channel [9,20]. Saedodin et al. [21] conducted a numerical analysis to assess the impact of porous metal foam on the thermal performance of FPSC, employing the local thermal equilibrium (LTE) assumption and implementing a semi-filled porous substrate arrangement in the FPSC channel. The examination of heat transfer and pressure drop within the FPSC channel substantiated that the introduction of porous substrate has the potential to increase the maximum thermal efficiency and global Nusselt number (*Nu*) by 18.5% and 82%, respectively. The improvement in thermal performance of FPSC, achieved through the intermittent insertion of porous metal foam blocks, was numerically investigated under the assumption of the local thermal equilibrium (LTE) model in the porous regions [22]. In addition, in order to optimize the configuration of FPSC with porous blocks, the shape of the porous metal foam significantly impacts the thermal performance of FPSC [19]. Meanwhile, considering both heat transfer and pressure drop in the FPSC channel, it is imperative to analyze the performance evaluation criteria (PEC) comprehensively to assess the thermal performance of FPSC [23].

On the other hand, the development of highly efficient nanofluids in the FPSC channel is another favorable way, wherein the thermal efficiency of FPSC is significantly influenced by the properties of the working fluid [24]. In recent years, some literature reviews have been published in this field [1,14,15]. Safarian et al. [25] numerically studied the characteristics of heat transfer in a flat-plate solar collector using nanofluids in different concentrations (Al_2O_3/water and CuO/water). The findings demonstrated that the introduction of nanoparticles and altering the flow direction in the FPSC channel induce an increase in the convective heat transfer coefficient. This phenomenon has been previously observed by Gupta et al. Gupta et al. [26] numerically tested the thermal performance of FPSCs with and without nanofluid (Al_2O_3/water). The outlet water temperature of FPSC without nanofluid was 5–10 °C lower than that the nanofluid was used. Moreover, Darbari and Rashidi [27] conducted a numerical simulation to explore the thermal efficiency of a flat plate thermosyphon solar water heater using various nanofluids. The study incorporated the examination of different parameters, including the volume fraction of nanoparticles, volumetric flow rate, solar radiation intensity, and more. The findings revealed that among the diverse nanoparticles tested, the inclusion of copper nanoparticles, followed by copper oxide, led to the most substantial enhancements in efficiency and useful energy. Esmaeili et al. [28] proposed an innovative solar collector design incorporating copper oxide (CuO) porous foam and nanoparticles with superior optical properties, aiming to enhance the thermal performance of the FPSC. Taking into account varying nanoparticle volume fractions, foam pore sizes, working fluid mass flow rates, as well as different thicknesses and positions of the porous layer within the FPSC channel, the numerical findings revealed that the efficiency of FPSC, whether partially or fully filled with metal foam, reached its peak value in the fully filled configuration. Additionally, compared with the water flow, the utilization of CuO nanofluid and metal foam led to an enhancement in collector efficiency by as much as 26.8% and 23.8%. Xiong et al. [29] conducted a numerical investigation exploring the impacts of hybrid nanofluid concentration (Ag-Al_2O_3/water), porosity, Darcy number, Reynolds number, and other factors that significantly influence the thermal performance of FPSC. Abolfazl et al. [30] propose solutions to improve the thermal performance of paraffin as a Phase-change Material (PCM) in solar flat-plate collector systems for domestic and industrial solar applications. Three methods are proposed: using 10 PPIs aluminum foams with 0.92 or 0.95 porosity, various types of 5%wt nanoparticles, and modifications to the geometry in three configurations: straight, wavy wall, and wavy wall Y-shaped fin combinations. The paper found that nano-powders reduce melting time by 18.15% and 40.70%, while metal foams or nanoparticles with foams improve cycling times.

It is clear from the review of the prior state-of-the-art presented above that using porous media and nanofluids improves the heat transfer of FPSC. In the present work, a novel configuration design of FPSC with intermittently inserting porous blocks is proposed. And the main objective is to illustrate the effects of some key factors on the thermal performance of FPSC, in which the porous foam shape, permeability, Reynolds number, nanoparticle type (Cu, Al_2O_3), volume fraction, and mixing ratio of hybrid nanofluids are mainly taken into account. The global heat transfer (Nu_g) in the FPSC channel is clarified at various Reynolds numbers. Meanwhile, the dimensionless pressure drop (friction coefficient (f_m)) is disclosed. Lastly, an analysis of the performance evaluation criteria (PEC) in the FPSC channel is conducted to identify an optimal configuration and operating parameters that yield maximum thermal efficiency.

2. Mathematical Model

2.1. Mathematical Model and Assumptions

The model employed in this investigation predominantly relies on an experimental prototype featuring channel dimensions of 13 mm (H) by 800 mm (L). [21]. Presuming the composite plate as a singular layer and overlooking the thickness and optical properties of the glass coverings and absorber plates [20]. Additionally, the lower wall of the FPSC channel is thermally insulated. The accurate magnitude of the geographical inlet radiation at any point can be ascertained by assuming that the solar radiation intensity remains consistent with the constant heat source on the absorber plate (q_w = 800 W/m^2) [9,31]. The base fluid within the channel is water (Pr = 7), and for the purposes of this study, the different types of nanoparticles (Al_2O_3-H_2O, Cu-H_2O), nanoparticle volume fraction (φ = 1%, 2%, and 3%), and hybrid nanofluid mixing ratios (0%Cu/100%Al_2O_3, 25%Cu/75%Al_2O_3, 50%Cu/50%Al_2O_3, 75%Cu/25%Al_2O_3, and 100%Cu/0%Al_2O_3) have been designed to study the effects of the new type of heat exchanger. The influence of the Reynolds number on the thermal performance of the FPSC is examined as the incoming fluid enters the collector with uniform velocity (u_{in}) and constant temperature (T_{in}). It is presumed that the fluid flow inside the channel is laminar, stable, and incompressible. Also, the effects of its radiation and buoyancy are not taken into account. In this study, the geometric shapes of the porous media are constructed as rectangles (REC), trapezoids (TRA_1, TRA_2), and triangles (TRI), as shown in Figure 1. Inserting porous media into the FPSC channel is designed to investigate the impact of body shape and permeability ($Da = 10^{-5}$~10^{-2}) within the FPSC channel. In addition, the porous metal foam is constructed from isotropic alumina (Al_2O_3) material with a consistent distribution of pores. Its thermophysical properties are presumed to remain constant, as outlined in Table 1.

Table 1. Parametric characteristics of porous media block.

Parameters	Value	Unit
Total length	0.36	m
Height	0.0078	m
Density	3.5×10^3	kg/m^3
Thermal conductivity	29	W/(m·K)
Specific heat capacity	750	J/(kg·K)
Darcy number	$Da = 10^{-5}, 10^{-4}, 10^{-3}, 10^{-2}$	
Material type	Al_2O_3	

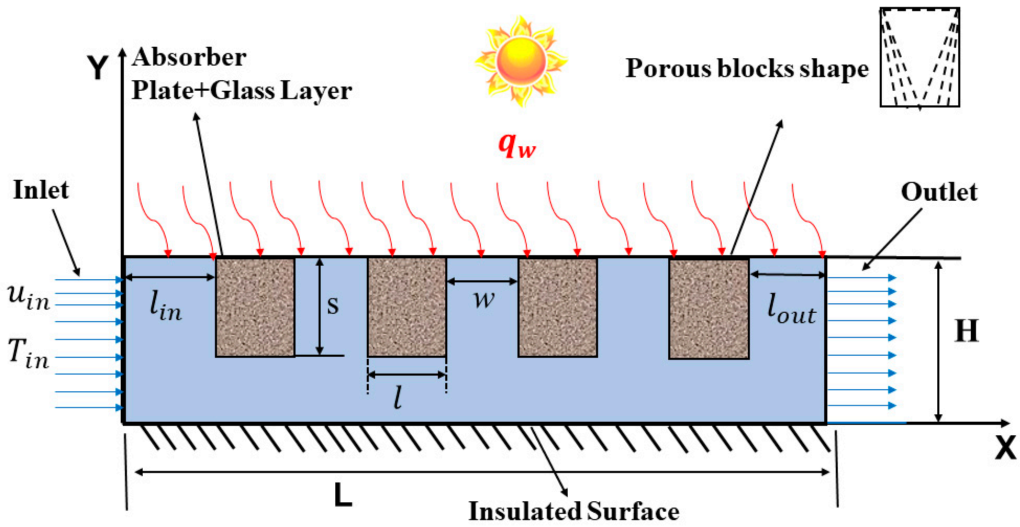

Figure 1. Schematic of the computational model for FPSC inserted with intermittent porous blocks.

2.2. Governing Equations

The Darcy–Brinkman–Forchheimer model [32] is employed to characterize the dissipation term in the momentum equation, considering the assumptions mentioned earlier. This model takes into consideration the influences of fluid viscous force and inertia force within the porous medium region of the collector. Additionally, the local thermal equilibrium (LTE) single-temperature model is utilized to describe the heat transfer between solids and fluids in proximity to the porous medium region [21]. In conclusion, the expression of the 2D mathematical governing equations is as follows.

Continuity Equation:

$$\frac{\partial u}{\partial x} + \frac{\partial v}{\partial y} = 0 \tag{1}$$

where u and v represent the velocity components in the x and y directions, respectively.
Momentum equations:

1. Governing equations in the fluid domain.

$$\rho\left(u\frac{\partial u}{\partial x} + v\frac{\partial u}{\partial y}\right) = -\frac{\partial p}{\partial x} + \mu\left(\frac{\partial^2 u}{\partial x^2} + \frac{\partial^2 u}{\partial y^2}\right) \tag{2}$$

$$\rho\left(u\frac{\partial v}{\partial x} + v\frac{\partial v}{\partial y}\right) = -\frac{\partial p}{\partial y} + \mu\left(\frac{\partial^2 v}{\partial x^2} + \frac{\partial^2 v}{\partial y^2}\right) \tag{3}$$

2. Governing equations in the porous medium domain.

$$\frac{\rho}{\varepsilon^2}\left(u\frac{\partial u}{\partial x} + v\frac{\partial u}{\partial y}\right) = -\frac{\partial p}{\partial x} + \frac{\mu_{eff}}{\varepsilon}\left(\frac{\partial^2 u}{\partial x^2} + \frac{\partial^2 u}{\partial y^2}\right) - \frac{\mu}{K}u - \frac{\rho F}{\sqrt{K}}\left|\vec{V}\right|u \tag{4}$$

$$\frac{\rho}{\varepsilon^2}\left(u\frac{\partial v}{\partial x} + v\frac{\partial v}{\partial y}\right) = -\frac{\partial p}{\partial y} + \frac{\mu_{eff}}{\varepsilon}\left(\frac{\partial^2 v}{\partial x^2} + \frac{\partial^2 v}{\partial y^2}\right) - \frac{\mu}{K}v - \frac{\rho F}{\sqrt{K}}\left|\vec{V}\right|v \tag{5}$$

where $\left|\vec{V}\right| = \sqrt{u^2 + v^2}$ is the combined velocity of transverse and longitudinal, ε is the porosity, and K is the permeability of the porous medium. Other variables include ρ for fluid density, p for fluid pressure, μ for dynamic viscosity, and μ_{eff} for effective viscosity. $F = \frac{1.75}{\sqrt{150}} \cdot \frac{1}{\varepsilon^{1.5}}$ is the inertial factor [33].

The permeability of porous media can be obtained by using the Carman–Kozeny formula [34].

$$K = \frac{D_p^2 \varepsilon^3}{180(1-\varepsilon)^2} \tag{6}$$

where D_p represents the pore diameter of the porous media matrix, and K is the permeability of a porous metal foam block, which is defined as follows:

$$K = Da \cdot {D_h}^2 \tag{7}$$

where D_h denotes the equivalent diameter of the channel.

Energy equation:

$$\frac{1}{\varepsilon}\left(u\frac{\partial T}{\partial x} + v\frac{\partial T}{\partial y}\right) = \tau\left(\frac{\partial^2 T}{\partial x^2} + \frac{\partial^2 T}{\partial y^2}\right) \tag{8}$$

where T is the temperature, and τ is the thermal diffusivity.

2.3. Boundary Conditions

In the present study, the boundary conditions are provided as follows:

FPSC inlet conditions:

$$u = u_{in}, v = 0, T = T_{in}, \nabla p = 0 \tag{9}$$

FPSC outlet conditions:

$$v = 0, \frac{\partial u}{\partial x} = 0, \nabla T = 0, p = 0 \tag{10}$$

An adiabatic condition is assumed to have a no-slip condition at the bottom wall of the collector channel.

$$u = v = 0, \nabla T = 0, \nabla p = 0 \tag{11}$$

Solar radiation is emitted via the top of the collection channel, and it is evenly dispersed over the absorber under no-slip conditions.

$$u = v = 0, \nabla T = -\frac{q_w}{k_{eff}}, \nabla p = 0 \tag{12}$$

where k_{eff} is the effective thermal conductivity, which is defined as follows [34].

$$k_{eff} = \varepsilon k_f + 0.195(1-\varepsilon)^{0.763} k_p \tag{13}$$

where k_f is the thermal conductivity of the fluid, and k_p is the thermal conductivity of porous media.

2.4. Nanofluid Parametric Definitions

From the thermal physical property parameters of heat transfer fluids, this paper looked into and sorted out the current standard calculation techniques for physical property parameters. The calculation models for thermal conductivity, specific heat capacity, and dynamic viscosity of nanofluids are proposed as follows.

Local heat balance energy equation of nanofluid flowing through porous metal foam block [35]:

$$\nabla \cdot (\rho_{nf} \vec{V} C_{p,nf} T) = \nabla \cdot (k_{eff,nf} \nabla T) \tag{14}$$

where the suffix n_f denotes the nanofluid, ρ is the fluid density, and C_p is the specific heat capacity of the nanofluid.

For the single-phase mixed model, the single nanoparticle density is as follows [35]:

$$\rho_{nf} = (1-\varphi)\rho_f + \varphi \rho_{np} \tag{15}$$

where φ is the volume fraction of the nanoparticle, n_p denotes the nanoparticle, and ρ_{np} is the density of the nanoparticle.

Thus, the thermodynamic properties of single nanoparticles can be calculated [35]:

$$\Omega_{np} = \varphi \Omega_s \tag{16}$$

where Ω is the specific property of the nanoparticle. Assuming the thermal balance between suspended nanoparticles and fluid, the viscosity (μ), thermal conductivity (k), and specific heat capacity (C_p) of a single nanoparticle can be calculated based on the calculations of [36]:

$$\mu_{nf} = \mu_f \left(1 + 0.025\varphi + 0.015\varphi^2\right) \tag{17}$$

$$k_{nf} = 0.25\left[(3\varphi - 1)k_{np} + (2 - 3\varphi)k_f + \sqrt{\Delta}\right] \tag{18}$$

$$C_{p,nf} = \frac{(1-\varphi)\left(\rho C_p\right)_f + \varphi\left(\rho C_p\right)_{np}}{\rho_{nf}} \tag{19}$$

where $\Delta = \left[(3\varphi - 1)k_{np} + (2 - 3\varphi)k_f\right]^2 + 8k_{np}k_f$.

The viscosity determines the Reynolds number value, and the Reynolds number and Prandtl number in the channel are defined as follows:

$$Re = \frac{4\dot{m}}{\pi H \mu} \tag{20}$$

$$Pr = \frac{\mu C_p}{k} \tag{21}$$

where $\dot{m}$ is the mass flow rate.

According to the formula for the thermodynamic properties of single nanoparticles, the thermodynamic properties of mixed nanoparticles can be deduced as follows [35]:

$$\Omega_{np} = \left(\frac{\varphi_c}{\varphi}\right)\Omega_c + \left(\frac{\varphi_a}{\varphi}\right)\Omega_a \tag{22}$$

where a and c represent Al_2O_3 nanoparticles and Cu nanoparticles, respectively. The volume fraction of nanoparticles is defined as follows:

$$\varphi = \varphi_a + \varphi_c \tag{23}$$

Density of mixed nanoparticles:

$$\rho_{hnf} = (1 - \varphi_a - \varphi_c)\rho_f + (\varphi_a + \varphi_c)\rho_{np} \tag{24}$$

where h_{nf} is the mixed nanoparticle, while the density of the mixed nanoparticles is

$$\rho_{np} = \left(\frac{\varphi_a}{\varphi}\right)\rho_a + \left(\frac{\varphi_c}{\varphi}\right)\rho_c \tag{25}$$

From this, the viscosity (μ), thermal conductivity (k), and specific heat capacity (C_p) of the mixed nanoparticles can be calculated:

$$\mu_{hnf} = \frac{\mu_f}{\left[1 - (\varphi_a + \varphi_c)\right]^{2.5}} \tag{26}$$

$$\frac{k_{hnf}}{k_f} = \frac{\left(\frac{\varphi_a k_a + \varphi_b k_b}{\varphi_{hnf}}\right) + 2(\varphi_a k_a + \varphi_b k_b) - 2k_f\varphi_{hnf} + 2k_f}{\left(\frac{\varphi_a k_a + \varphi_b k_b}{\varphi_{hnf}}\right) - (\varphi_a k_a + \varphi_b k_b) - 2k_f\varphi_{hnf} + 2k_f} \tag{27}$$

$$C_{p,hnf} = \frac{(1 - \varphi_a - \varphi_c)\left(\rho C_p\right)_f + \varphi_a C_{p,a}\rho_a + \varphi_c C_{p,c}\rho_c}{\rho_{hnf}} \tag{28}$$

2.5. Collector Control Parameters

The non-dimensional pressure drop's friction coefficient in the collector is defined as follows [20]:

$$f_m = \frac{2H\Delta p}{\rho u^2 L} \tag{29}$$

where f_m is the friction coefficient, H represents the height of the collector channel, and L denotes the length of the collector channel.

The definition of the local Nusselt number is as follows [21]:

$$Nu = \frac{hH}{k} = \frac{q_w H/k_f}{T_w - T_m} \tag{30}$$

where Nu represents the Nusselt number, h is the convective heat transfer coefficient, T_w is the wall temperature, and T_m is the mean volume temperature of the fluid. The latter can be calculated using the following formula [21]:

$$T_m = \frac{\int_{y=0}^{y=H} uTdy}{\int_{y=0}^{y=H} udy} \tag{31}$$

The mean Nusselt number within the porous media domain is determined as follows:

$$Nu_{mi} = \frac{1}{I}\int_{X_i}^{X_i+I} NudX \tag{32}$$

where I denotes the width of each porous block, and X_i signifies the inlet spatial location of each porous block.

The definition of the global Nusselt number in the FPSC is as follows:

$$Nu_g = \frac{\sum_{i=1}^{i=N} Nu_{mi}}{N} \tag{33}$$

where Nu_g denotes the global Nusselt number, while N signifies the count of porous blocks within the channel. Through the measurement of the incoming and outgoing temperatures of the working fluid, the net rate of effective heat absorption by the working fluid can be determined using the following formula [37]:

$$\dot{Q}_u = \dot{m}C_p(T_{out} - T_{in}) \tag{34}$$

In this context, $\dot{Q}_u$ represents the rate at which beneficial heat is acquired, with T_{out} and T_{in} denoting the temperatures of the working fluid as it exits and enters the solar collector, respectively.

The thermal efficiency is characterized as the proportion of extracted energy that is beneficial to the input solar energy. Considering that this study is a 2D model, the thermal efficiency per unit area of the solar collector can be defined according to Equation (34) as [37]

$$\eta = \frac{\dot{Q}_u}{q_w A_c} = \frac{\dot{m}C_p(T_{out} - T_{in})}{q_w A_c} \tag{35}$$

where A_c is the collector unit lighting area.

3. Numerical Details

3.1. Numerical Method

All simulations in this investigation were run using the finite volume method-based ANSYS Fluent 19.1 software. The governing equations were numerically and discretely solved using the finite volume approach. The coupling of velocity and pressure is determined using the SIMPLE technique, and the momentum and energy equations are adopted in second-order upwind format for stability. The largest iterative residual of all variables below 10^{-8} is recognized as convergence criteria are established, and for the steady-state flow issue in this study, the laminar flow model is also adopted.

3.2. Grid Independence Validation

A grid independence assessment was conducted for the model using the subsequent parameters: Da = 10^{-4}, Re = 234, s = 0.6 H, the porous block was rectangular, water served as the heat transfer fluid within the channel, and the parameter s was set to 0.6 H to validate the precision of the numerical solution. Figure 2 illustrates the changes in the total Nusselt number and friction coefficient with various grid positions. With more grid points, we observe a drop in Nu_g and f_m. The channel Nu_g and f_m curves tend to stabilize when the grid points rise to 150 × 1000. In this instance, the global Nusselt number and channel friction coefficient are not significantly impacted by changes in the grid points. Therefore, it may be said that 150 × 1000 is the ideal mesh size. In addition, Table 2 conducts a comparison between the aforementioned model and the empty channel while taking the effect of various mesh sizes on channel outlet temperature (T_{out}) into account. The results show that the percentage difference between the porous block and non-porous block in the NO.3 channel is 0.5% and 0.4%, respectively, while that of the NO.4 channel is 0.08% and 0.09%, respectively; this is computed using the expression, i.e., the percentage error = $\left(Nu_{g(No.n+1)} - Nu_{g(No.n)}\right)/Nu_{g(No.n+1)}$. Therefore, with the above two verification methods, it can be confirmed that the grid point selection of 150 × 1000 can obtain sufficient accuracy.

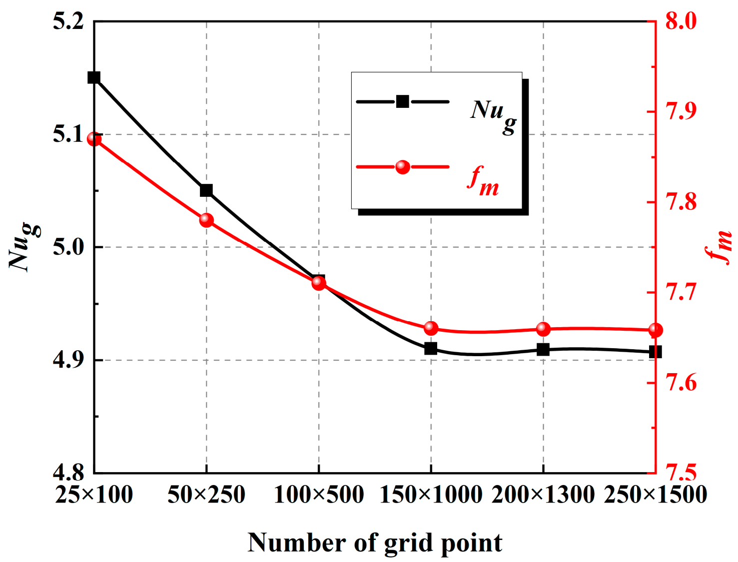

Figure 2. Verification of grid independence through the utilization of the Nusselt number and friction.

Profiles of the coefficient in the FPSC channel: Da = 10^{-4}, Re = 234, and s = 0.6 H.

Table 2. Analysis of the sensitivity of the channel exit temperature to different meshing schemes.

No.	Grid Size	T_{out} s = 0	Percentage Difference (%)	s = 0.6 H, Re = 234, Da = 10^{-4}	Percentage Difference (%)
1	25 × 100	292.9		295.7	
2	50 × 250	296.4	1.20	300.4	1.60
3	100 × 500	297.9	0.50	301.6	0.40
4	150 × 1000	298.2	0.08	301.9	0.09
5	200 × 1300	298.4	0.06	302.2	0.08
6	250 × 1500	298.5	0.05	302.4	0.07

3.3. Numerical Verification

To enhance the credibility of the numerical approach utilized in this investigation, Figure 3 provides a comparative assessment of the computed average Nusselt number and friction factor against results documented in the existing literature [21]. It is essential to note that, for the sake of calculation accuracy, a grid resolution of 150 × 1000 was used for the channel area. Comparative error analysis between the results of this study and those from Saedodin's study reveals that under various conditions, such as mass flow rates at the inlet of 0.5 L/min (Re = 234), 1.0 L/min (Re = 351), and 1.5 L/min (Re = 468), the differences in the calculated results are not significant. The greatest relative errors of Nu_g and f_m are 2.23% and 1.35%, respectively, which can attest to the validity of this study's numerical method. It can be demonstrated that the results of this study's numerical calculations are trustworthy enough by the double verification of mesh size and numerical approach. As a result, the following numerical investigations employ this numerical approach.

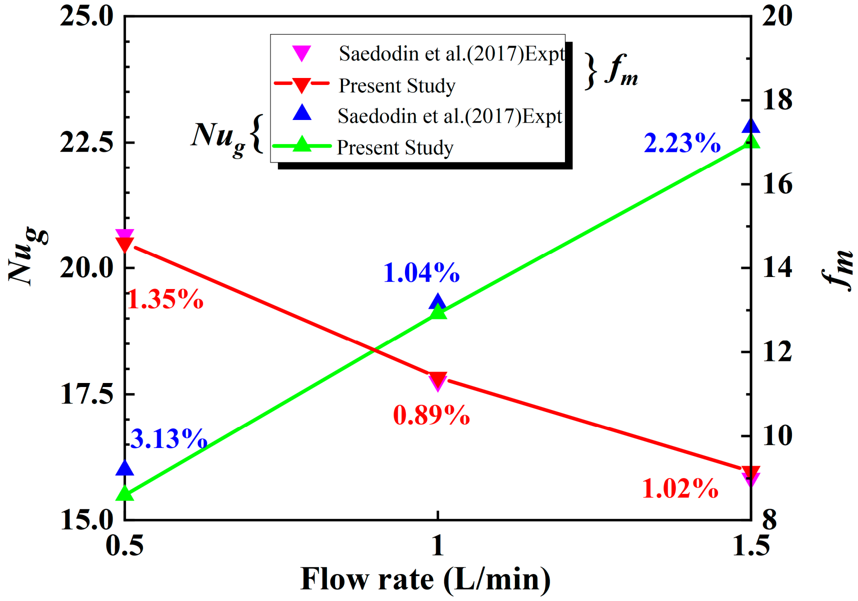

Figure 3. Comparison of FPSC channel average Nusselt number (Nu_g) and friction coefficient (f_m) with the experimental data [21].

4. Results and Discussions

4.1. Heat Transfer Performance and Resistance Loss of the Collector

In order to precisely assess the improved heat transfer characteristics in FPSC channels with porous media and nanofluids, this section conducts a separate examination of the dimensionless analysis of the global Nusselt number under the aforementioned influential factors. Additionally, the introduction of porous blocks into FPSC substantially improves heat transfer performance; however, it simultaneously leads to an increase in resistance, leading to higher energy dissipation effects. Therefore, considering these aforementioned factors, a comprehensive analysis of the characteristics of resistance loss in FPSC channels with inserted porous blocks is imperative. As a dimensionless parameter linked to the permeability of porous media, the Darcy number ($Da = K/D_p{}^2$) was calculated using the empirical Equation (6). To examine the impact of various Da values of porous blocks on the flow within FPSC channels, Figure 4 depicts the changes in the global Nusselt number (Nu_g) in the FPSC channel under the base fluid condition (water) with different permeability shapes of porous blocks. Clearly, it is noticeable that, for a specific shape of the porous block, Nu_g rises with an increase in Da, and vice versa. This is due to the fact that at higher permeability (Da = 10^{-2} and Da = 10^{-3}), more fluid passes through the interior of the porous block, enhancing heat exchange. Furthermore, for porous blocks with the same Da values, the configuration of the porous block also exerts a noteworthy influence on

Nu_g, exhibiting an almost monotonic increase as the shape transitions from a triangle (TRI) to a rectangle (REC). It is worth noting that the shape changes of TRI and TRA_2 porous blocks have little effect under low *Da* ($Da = 10^{-4}$ and $Da = 10^{-5}$) conditions. This is because the rectangular shape of the porous block provides a larger solid–liquid heat exchange area compared to the triangular and trapezoidal shapes. Additionally, a close examination of Figure 4a,b reveals that the Nu_g of the channel at $Re = 468$ exhibits a higher value in comparison to the base fluid at $Re = 234$. According to Equation (20), as *Re* increases, fluid velocity accelerates, leading to an increase in Nu_g. In a comprehensive comparison and analysis of the results in Figure 4, it is evident that under the conditions of base fluid $Re = 468$ and a $Da = 10^{-2}$ for REC porous blocks, the heat transfer efficiency within the FPSC channel is at its peak, attaining a maximum Nu_g value of 7.20.

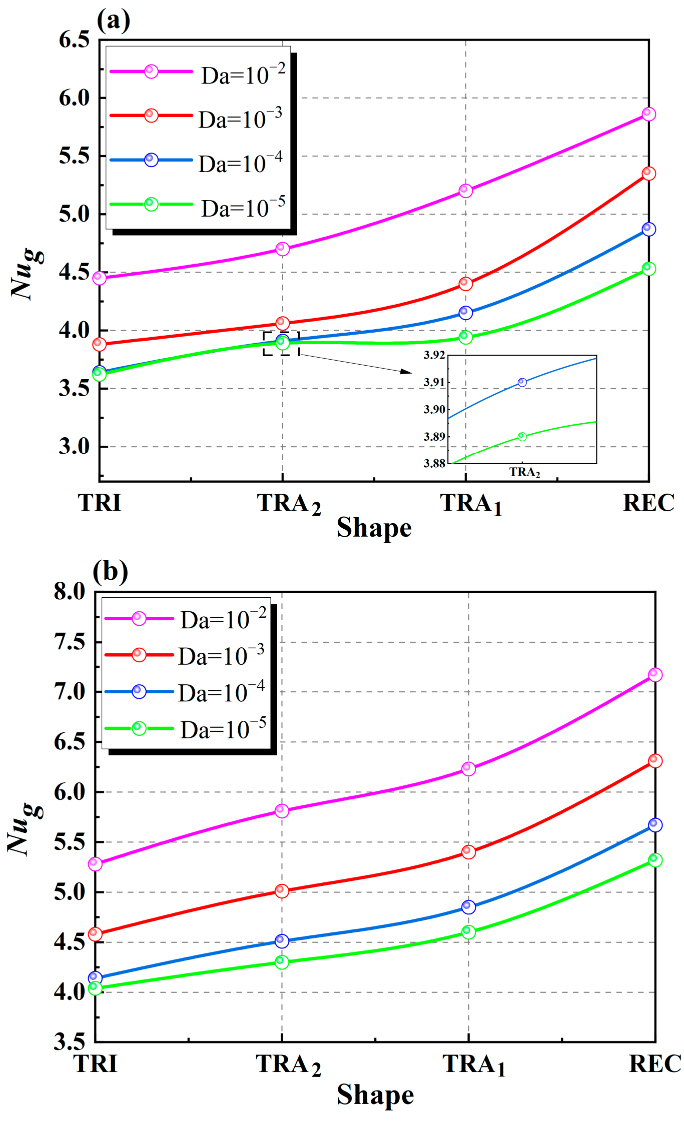

Figure 4. Variation of the global Nusselt number (Nu_g) in the FPSC channel with the shape change of inserted porous blocks at various *Da* and Reynolds numbers (*Re*): (**a**) $Re = 234$; (**b**) $Re = 468$.

Figure 5 illustrates the variations in the dimensionless pressure drop friction coefficient (f_m) for the same operating conditions as depicted in Figure 4. It showcases the non-linear behavior of the in-channel friction coefficient (f_m) concerning different porous block (Al_2O_3) shapes, Darcy numbers, and Reynolds numbers (*Re*). It is evident that, for a specified configuration of a porous block, when its *Da* number diminishes while maintaining a constant pore diameter, the porosity and pore density (PPI) also decrease, resulting in elevated permeability resistance loss and an inevitable increase in the friction coefficient as per Equation (6). Additionally, the friction coefficient (f_m) demonstrates an almost linear escalation as the configuration of the inserted porous block transitions from TRI to REC. Specifically, the REC porous block, maintaining an equivalent base width dimension, occupies the most extensive channel space compared to the TRA- and TRI-shaped porous blocks. As a result, fluid flow through the porous media matrix experiences greater viscous and inertial resistance, leading to the largest in-channel pressure drop and the highest f_m value. Moreover, a comprehensive comparative analysis of Figure 5a,b reveals that, under low Reynolds number (Re = 234) conditions, the f_m value is consistently higher than that observed under high Reynolds number conditions (Re = 468). The variation can be ascribed to the reduced flow rate within the FPSC channel under the condition of low Reynolds number, resulting in lower inlet kinetic energy and, thus, a relatively higher calculated value of the f_m. In summary, it is apparent that the f_m maximum value of 7.91 is attained in the case of the REC porous block with $Da = 10^{-5}$ and Re = 234.

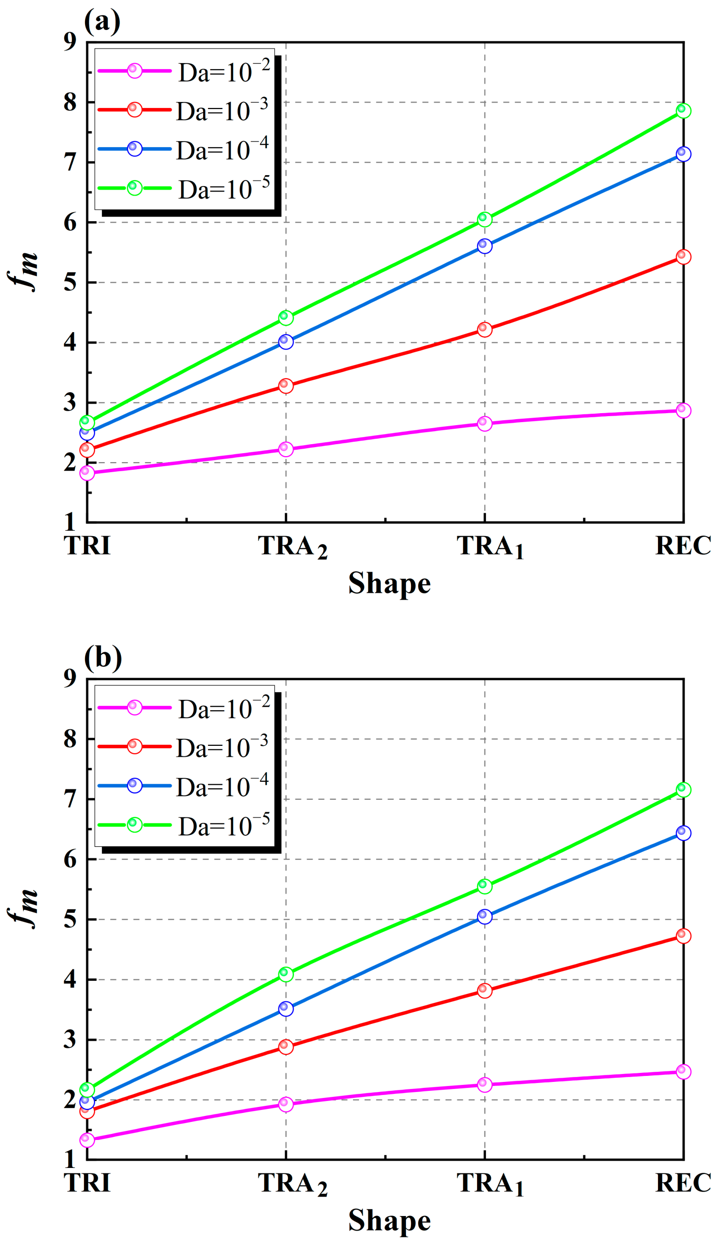

Figure 5. Variation of the friction coefficient (f_m) in the FPSC channel with the shape change of inserted porous blocks at various Da and Reynolds numbers (Re): (**a**) Re = 234; (**b**) Re = 468.

To delve deeper into the impact of the Darcy number (Da) of the porous block on the Nusselt number (Nu_g) and friction coefficient (f_m) within the channel, Figure 6 delves deeper into the analysis, building upon the findings from Figures 4 and 5. Figure 6 presents the impact of inserting REC porous blocks with Da values ranging from 10^{-7} to 10^{-1} on the channel Nu_g and f_m under the Re = 234 operating condition. It is evident that as Da increases from 10^{-7} to 10^{-2}, the channel Nu_g also increases. However, it is worth noting that as Da further increases to 10^{-1}, the Nu_g of the channel exhibits a decreasing trend.

This occurrence can be ascribed to the rise in porosity, resulting in a decrease in the available surface area for solid–liquid heat transfer between the fluid and the porous block, resulting in a decrease in Nu_g. This indicates that for Re = 234, the REC porous block with $Da = 10^{-2}$ yields the most favorable conditions for achieving the maximum value of FPSC channel Nu_g, which reaches a maximum value of 5.91. Furthermore, by examining Figure 6, it becomes apparent that the channel's f_m consistently decreases with an increase in the porous block Da. As a result, a minimum value of 1.01 is observed at $Da = 10^{-1}$ for the channel's f_m.

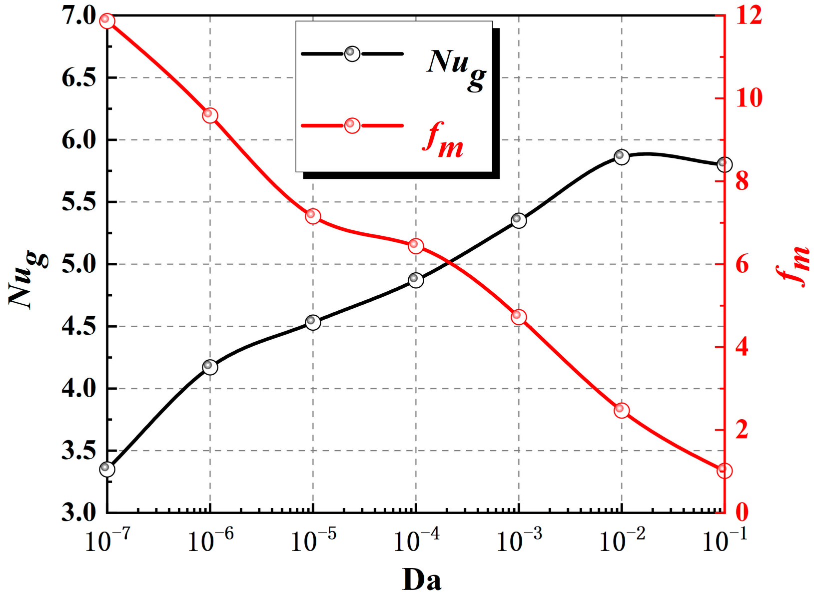

Figure 6. Variation of the Nusselt number (Nu_g) and friction coefficient (f_m) in the FPSC channel with the Da change of inserted porous blocks.

Considering the impact of the laminar fluid Reynolds number (Re) on both the heat transfer efficiency and pressure drop within the channel, Figure 7 depicts the influence of the Reynolds number (Re) of the base fluid on the Nusselt number (Nu_g) and pressure drop (ΔP) within the channel. This analysis is conducted under the operational scenario of an inserted porous block with a rectangular shape and $Da = 10^{-2}$. It is evident that the Nu_g and ΔP of the channel increase with rising fluid Re in the laminar flow regime. At a high Re value (Re = 2000), the channel achieves its maximum Nu_g and ΔP, which are 11.58 and 3.48.

In Figure 8, we investigate the influence of various nanoparticle species and volume fractions on the heat transfer efficiency of FPSC channels. This analysis is conducted under the conditions involving a porous block with a rectangular shape, $Da = 10^{-2}$, and fluid Re = 234. Figure 8a presents the variation of channel Nu_g with different volume fractions of Al_2O_3-H_2O nanofluids flowing through the FPSC channel. It is evident that higher Nu_g values are observed with increased volume fractions, and the maximum value is achieved with the REC porous block. This improvement can be ascribed to the augmentation resulting from the addition of Al_2O_3 nanoparticles, which contributes to an increase in the thermal conductivity, density, and viscosity of the fluid; a decrease in specific heat capacity; and a notable enhancement in heat transfer within the channel is observed in comparison to the base fluid, thereby amplifying the overall heat transfer efficiency of the channel. In

Figure 8b, the nanofluid is Cu-H_2O, and it is apparent that the inclusion of Cu nanoparticles also improves the heat transfer efficiency of the channel. A comparison between Figure 8a,b reveals that, under the same volume fraction condition, Cu-H_2O has a significantly higher impact on the channel's heat transfer performance compared to Al_2O_3-H_2O. In summary, under the conditions of an inserted rectangular-shaped porous block and an increased volume fraction of Cu-H_2O to 3%, the Nu_g within the channel attains its peak at a value of 6.80, signifying a notable improvement of 20.7% in comparison to the base fluid.

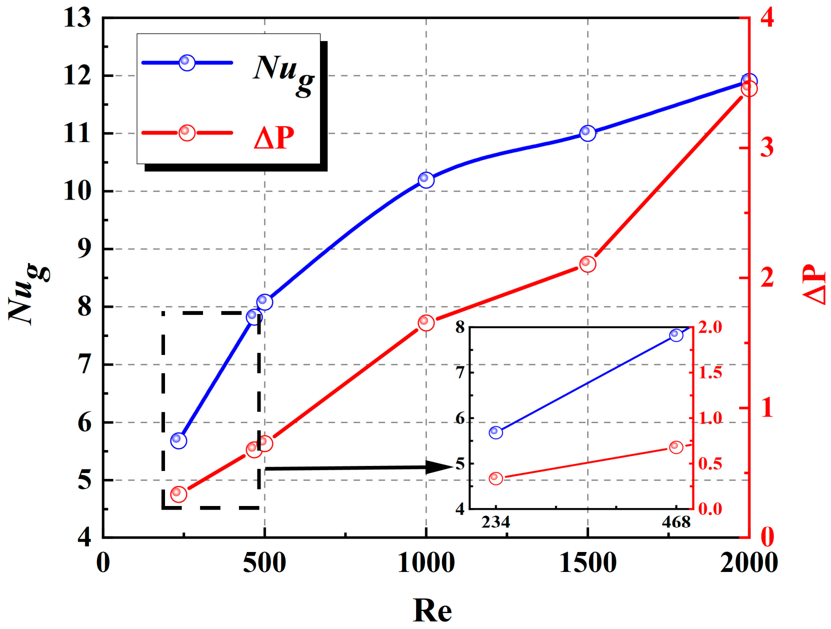

Figure 7. Variation of the Nusselt number (Nu_g) and pressure drop (ΔP) in the FPSC channel with the Reynolds number change.

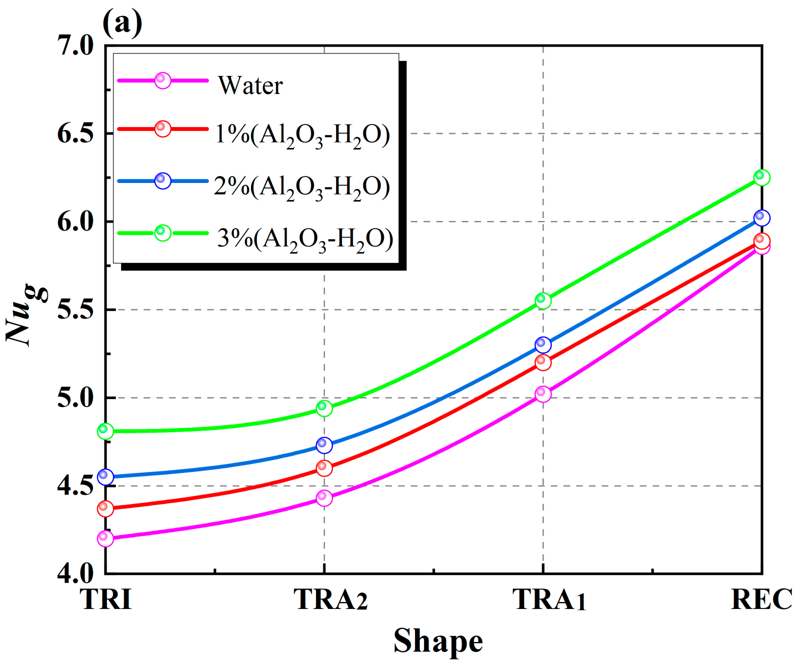

Figure 8. *Cont.*

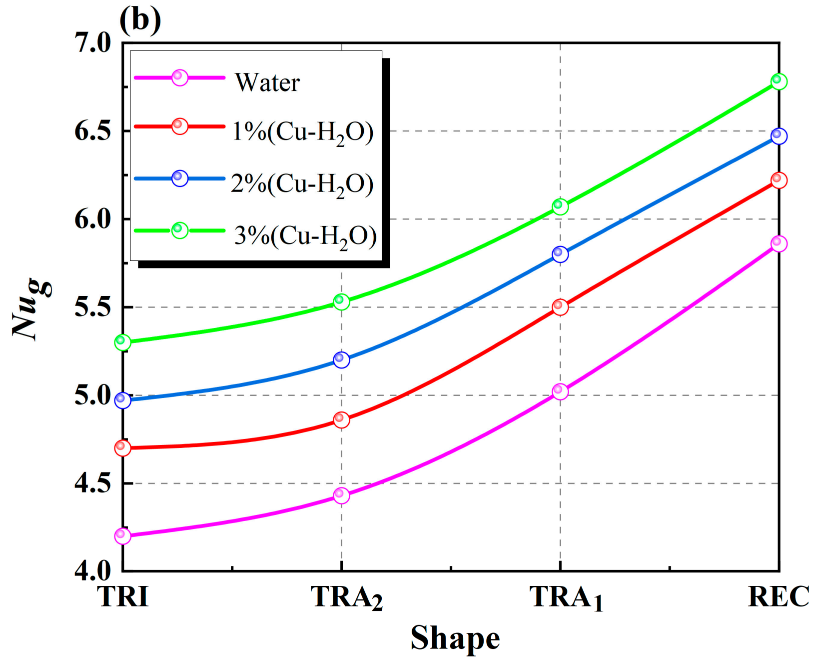

Figure 8. Variation of the global Nusselt number (Nu_g) in the FPSC channel with the shape change of inserted porous blocks in different kinds of nanofluids: (**a**) Al_2O_3-H_2O; (**b**) Cu-H_2O.

Nanofluids have the potential to significantly improve the heat transfer efficiency of the channel; however, they are also associated with an augmented level of frictional resistance. Figure 9 depicts the trends in frictional resistance loss corresponding to the conditions in Figure 8. Upon observation of Figure 9, it is evident that the addition of nanoparticles leads to an elevation in the channel's friction coefficient (f_m). This occurrence is a result of the elevated density and dynamic viscosity of the nanofluid when contrasted with the base fluid, increasing the channel's frictional losses. Additionally, an increase in nanoparticle volume fraction is accompanied by a corresponding rise in f_m. It is noteworthy that the rate of f_m increment gradually diminishes. This behavior is attributed to an increased presence of nanoparticles, which promotes improved mixing of the boundary layer, consequently reducing frictional resistance. Comparative analysis of Figure 9a,b reveals that, under the same volume fraction condition, the f_m for Cu-H_2O is slightly higher than that for Al_2O_3-H_2O. This difference can be explained by the significantly higher density of Cu-H_2O nanofluid in comparison to Al_2O_3-H_2O nanofluid. In summary, when the porous block takes a rectangular shape and the concentration of Cu-H_2O is increased to 3%, the channel's f_m reaches a maximum value of 3.96, representing a 33.8% increase in drag loss compared to an empty channel.

Figure 9 illustrates how the performance of the channel's heat transfer is affected in different ways by the inclusion of several types of nanoparticles. Based on this, more research is conducted to determine the effects of the simultaneous addition of two different types of nanoparticles and the mixing ratio on the channel's ability to transport heat. In Figure 10, the impact of the mixing ratio of Al_2O_3 and Cu nanoparticles (φ_c is the proportion of Cu nanoparticles) on the heat transfer efficiency of the FPSC channel is depicted. This analysis considers diverse nanoparticle volume fractions and porous block shapes, with the porous block (Al_2O_3) characterized by $Da = 10^{-2}$ and fluid $Re = 234$. The corresponding overall Nu_g number in the FPSC channel is big for the condition of a high Cu nanoparticle proportion ($\varphi_c = 100\%$), regardless of the nanoparticle volume fraction and the configuration of the porous block, exhibiting enhanced thermal performance. The Nu_g experiences a substantial increase when the configuration of the porous block transitions from TRI to REC. Additionally, the shape of the porous block will influence the mixing ratio of blended nanoparticles. It can be seen from the curve variation that the influence of the nanofluid mixing ratio on Nu_g increases with the change in the shape of the porous block: TRI-TRA-REC. Because more nanofluids flow through the porous block as it transforms from a triangle to a rectangle, the effect of nanofluid mixing becomes more substantial than that of Nu_g. This is the cause of the occurrence. Additionally, it is observed that, as the nanoparticle volume fraction increases from 1% to 3%, the shape of the porous block and the ratio of nanofluid mixing do not impact the extent to which the Nusselt number (Nu_g) of the channel increases. FPSC exhibits the best thermal performance when the mixing ratio of nanofluids is φ_c = 100% (Cu), and upon a comprehensive examination of the Nu_g depicted in Figure 10, it is noted that the Nu_g can attain a value of 6.80 within the channel when the shape of the porous block is rectangular and the nanoparticle volume fraction is 3%. The heat transfer performance is increased by roughly 13.3% when compared to φ_c = 0% (Al_2O_3).

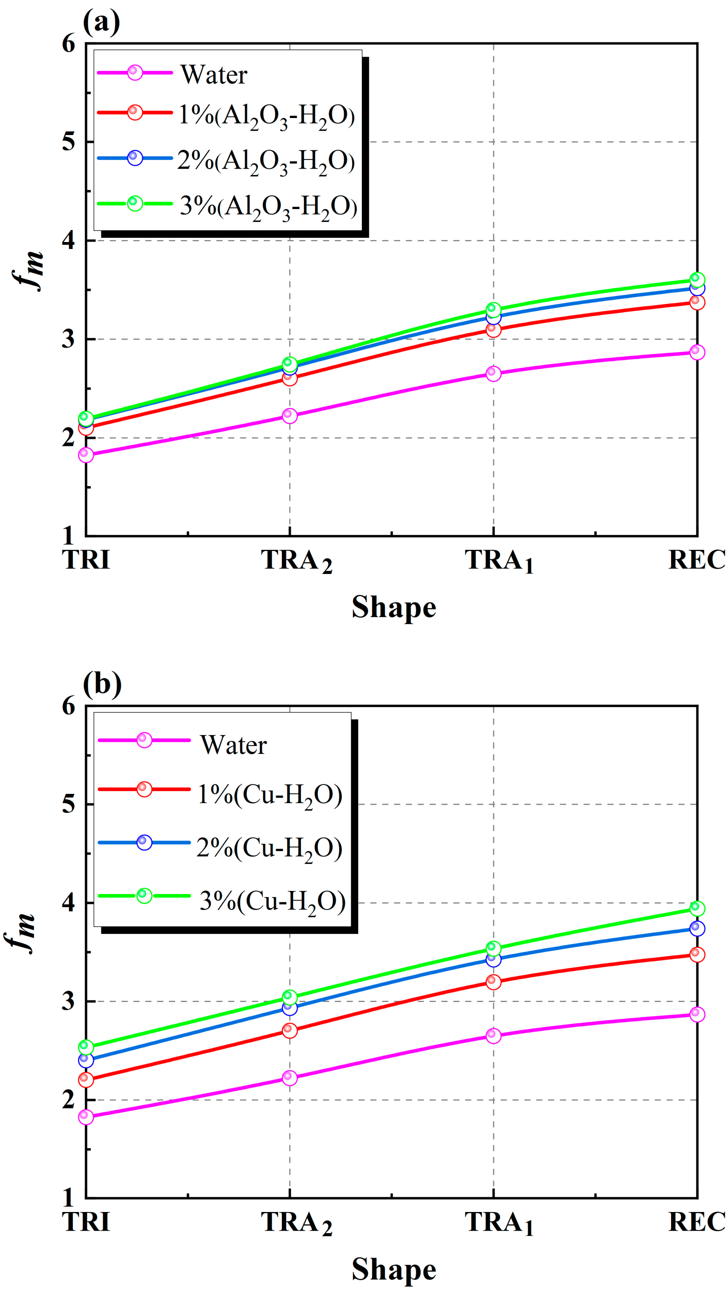

Figure 9. Variation of the friction coefficient (f_m) in the FPSC channel with the shape change of inserted porous blocks in different kinds of nanofluids: (**a**) Al_2O_3-H_2O; (**b**) Cu-H_2O.

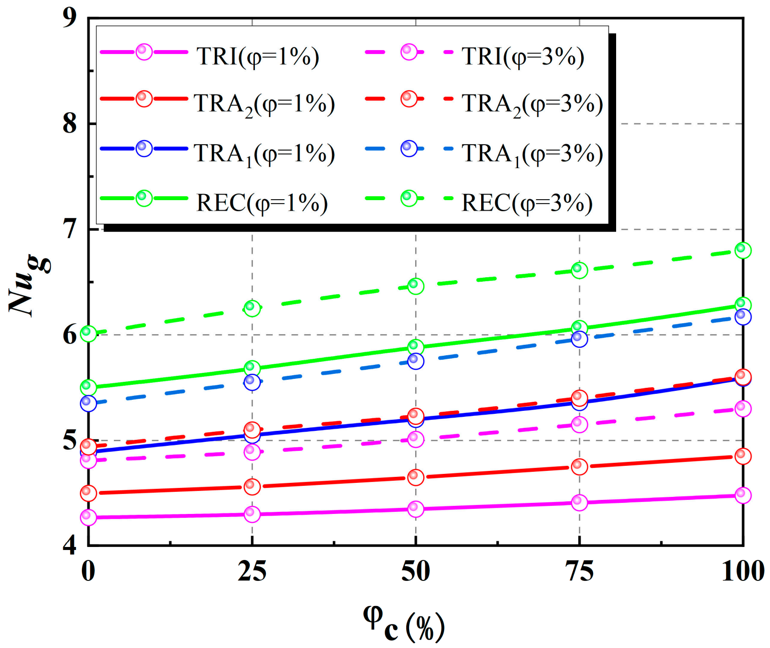

Figure 10. Variation of the global Nusselt number (Nu_g) in the FPSC channel with the shape change of inserted porous blocks in different volume fractions and mixing ratios of nanofluids.

4.2. Outlet Temperature of the Collector

To delve deeper into the impact of the factors mentioned above on the heat transfer efficiency of the FPSC channel, this study monitored the distribution of the channel's outlet temperature.

In Figure 11, the impact of porous block permeability on the distribution of the channel's outlet temperature is depicted. This analysis is conducted under the conditions of a rectangular porous block shape and a base fluid Re = 468. By applying both the median and interquartile range as measures of location, it becomes apparent that the temperature gradient near the insulating plate increases gradually, while in proximity to the collector plate, the temperature rise at the outlet is remarkably pronounced. This occurrence can be ascribed to the substantial disruption of flow patterns induced by the insertion of porous blocks into the channel. In this scenario, a majority of flow lines circumvent the porous blocks, resulting in the formation of recirculation vortex zones near the rear of each porous block. This phenomenon enhances the mixing of flow and heat, as compared to the empty channel. In Figure 11, it is also evident that the channel's outlet temperature gradient exhibits a consistent distribution trend under different permeability conditions. For the $Da = 10^{-2}$, the channel's outlet temperature gradient is significantly higher than that observed in cases with lower Darcy numbers (10^{-5}~10^{-3}). Furthermore, the channel's mean outlet temperature consistently ranks highest, followed by a gradual decrease in the mean outlet temperature as the Darcy number decreases. This observation indicates that the insertion of porous blocks with high Darcy numbers is advantageous for enhancing FPSC thermal performance. This effect is attributed to the high-resistance porous block, which restricts fluid flow through the porous block, resulting in limited heat exchange between the fluid and the collector plate, particularly near the absorber plate.

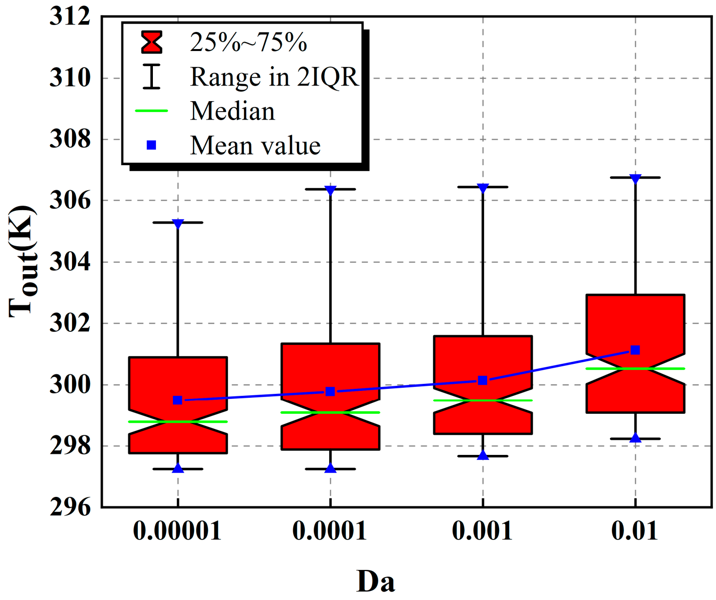

Figure 11. Comparisons of the outlet temperature of FPSC for the effects of various Darcy numbers at *Re* = 468.

In Figure 12, the alterations in the FPSC channel's outlet temperature are illustrated in relation to the shape of the porous block under the condition of $Da = 10^{-2}$. By applying both the median and interquartile range as measures of location, it is evident that, similarly to the operational conditions depicted in Figure 11, the outlet temperature gradient increases gradually in most locations at the channel's exit and significantly increases in a small area close to the collector. With an increase in volume fraction, the peak and valley values rise. In Figure 12a,b, the maximum observed outlet temperature peaks are 306.8 °C and 305.9 °C, respectively, when the porous block shape is REC. The average outlet temperature of the channel reaches its highest value when the porous block shape is REC in comparison to TRI and TRA, and the outlet temperature experiences a continuous increase as the shape of the porous block transitions from TRI to TRA to REC. Furthermore, upon comparing Figure 12a,b, it becomes evident that the average outlet temperature of the channel is higher when the Reynolds number is low ($Re = 234$) and vice versa. As a result, when the porous block is rectangular, $Da = 10^{-2}$ and $Re = 234$, and the fluid is the base fluid, the channel's average outlet temperature can achieve a peak value of 302.1 °C.

In Figure 13, the influence of nanoparticle volume fraction on the outlet temperature distribution of the FPSC channel is depicted under the conditions of a REC-shaped porous block with $Da = 10^{-2}$ and $Re = 234$. By examining the median and interquartile range of the data in Figure 13, it becomes evident that irrespective of the nanoparticle volume fraction, temperature valleys are consistently observed near the insulating plate, while temperature peaks occur in proximity to the upper collector plate. Furthermore, both the peaks and valleys exhibit an increase with higher nanoparticle volume fractions. In addition, the growth trend of the outlet temperature gradient in the vicinity of the upper collector plate is particularly pronounced, in contrast to the behavior of the outlet temperature gradient near the insulating plate. Additionally, it is evident that the average outlet temperature of the channel increases with a rise in nanoparticle volume fraction. Consequently, higher average exit temperatures are observed with higher volume fractions ($\varphi = 3\%$). Upon comparing Figure 13a,b, it can be observed that Cu-H_2O nanofluid, when flowing through the channel, results in a higher average exit temperature compared to Al_2O_3-H_2O. In summary, it is noteworthy that the conditions of REC porous block ($Da = 10^{-2}$, $Re = 234$) and Cu-H_2O nanofluid lead to a maximum average exit temperature of 303.1 °C for the channel.

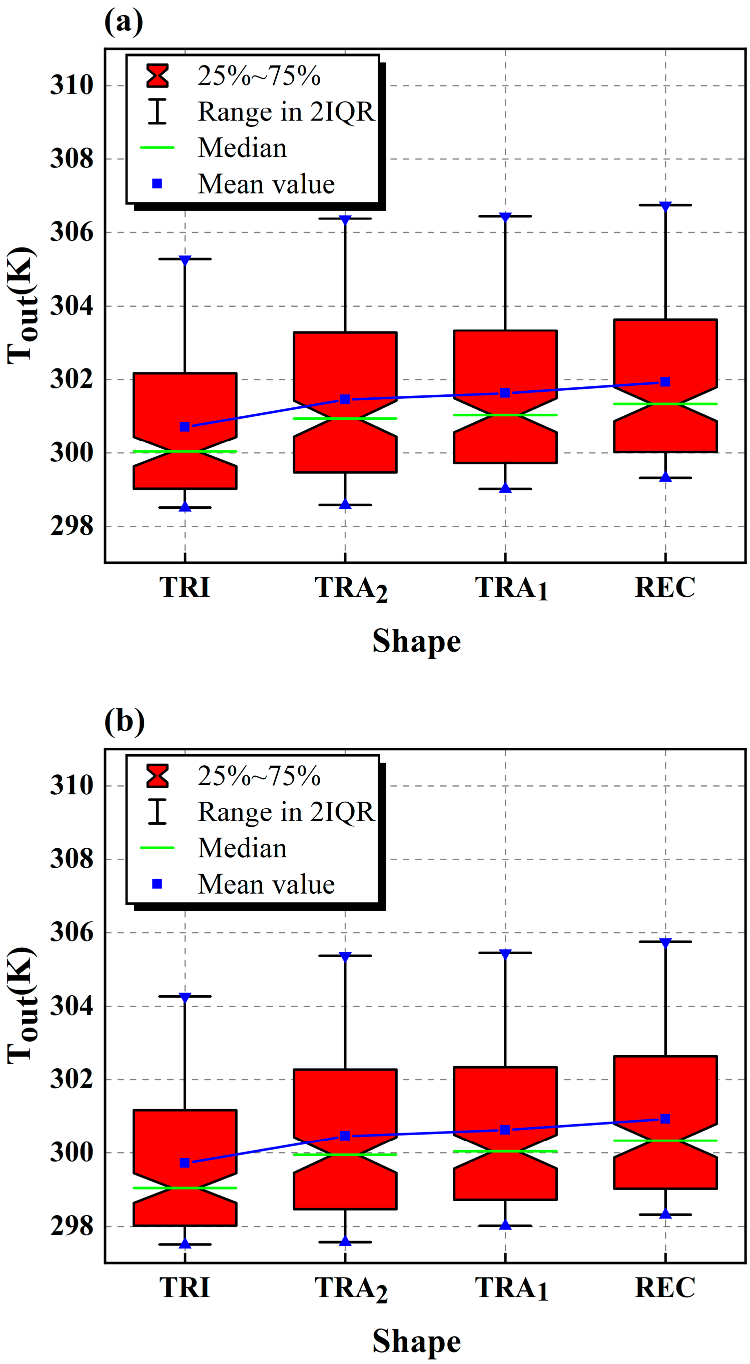

Figure 12. Comparisons of the outlet temperature of FPSC for the effects of different porous block shapes at various Reynolds numbers: (**a**) *Re* = 234; (**b**) *Re* = 468.

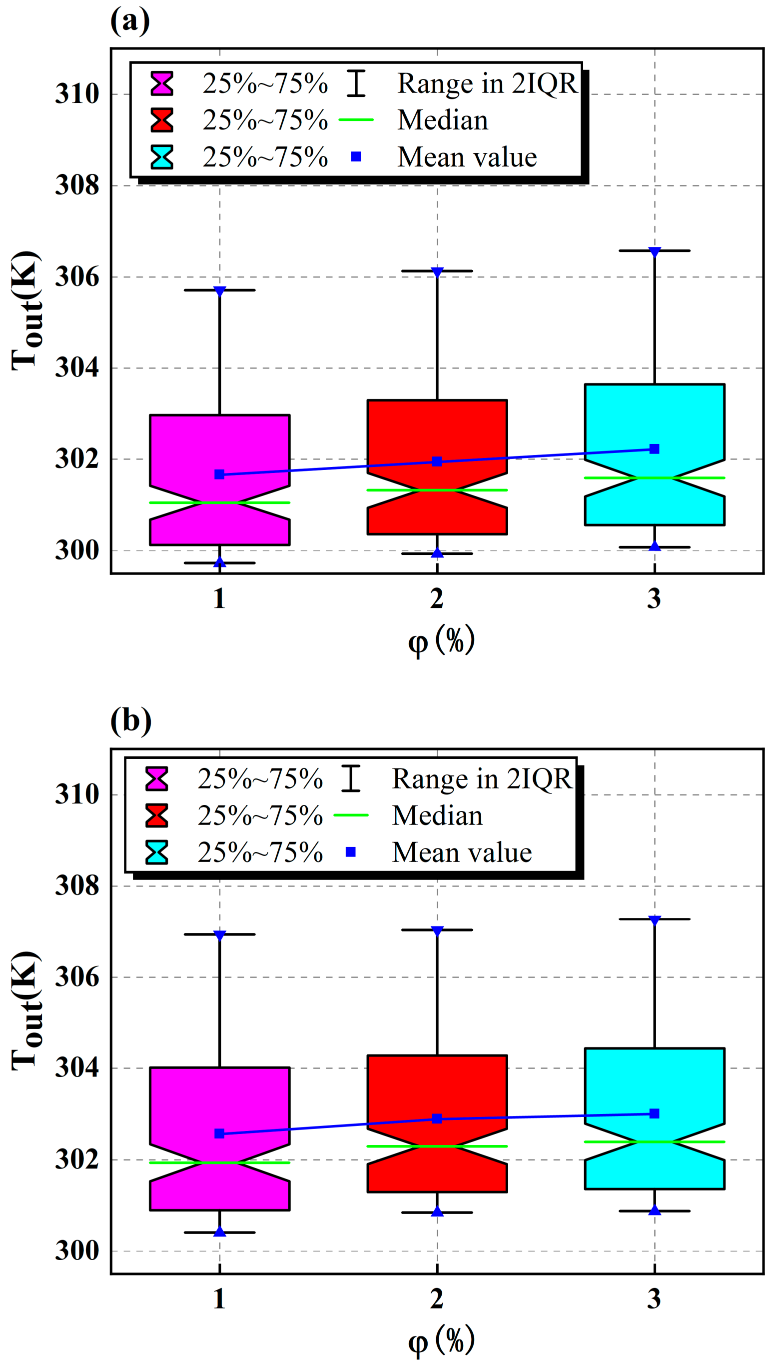

Figure 13. Comparisons of the outlet temperature of FPSC for the effects of different volume fraction nanofluids at various Reynolds numbers: (**a**) Re = 234; (**b**) Re = 468.

4.3. Thermal Efficiency of Solar Collector

The solar collector's thermal efficiency can be expressed by Equation (35), which is most simply understood as the ratio of useful heat output per unit area of the collector to the heat projected onto the collector surface. This equation serves as a means of evaluating the integrated thermal efficiency index of the solar collector system. Figure 14a demonstrates how the thermal efficiency of the FPSC channel is influenced by the shape and permeability of the porous block, with calculations performed at the base fluid Re = 234. As the Darcy number increases, the thermal efficiency of the collector proportionally rises, regardless of the configuration of the porous block shape; there is an additional observation that as the shape progresses from TRI-TRA-REC, the collector's thermal efficiency increases.

Therefore, the REC porous block, characterized by $Da = 10^{-2}$, demonstrates a peak thermal efficiency of 67%. Moreover, upon examination of Figure 14b, it is evident that the addition of nanoparticles significantly enhances the thermal efficiency of the collector, and this enhancement is positively correlated with the increase in the volume fraction of nanoparticles. When the added nanoparticles contain both Cu and Al_2O_3, a noteworthy observation is that a higher percentage of Cu nanoparticles results in a higher thermal efficiency for the collector. This indicates that at a nanoparticle volume fraction of 3% and $\varphi_c = 100\%$, the collector's thermal efficiency reaches a maximum value of 70.5%, representing a 2.5% increase compared to Al_2O_3 nanoparticles.

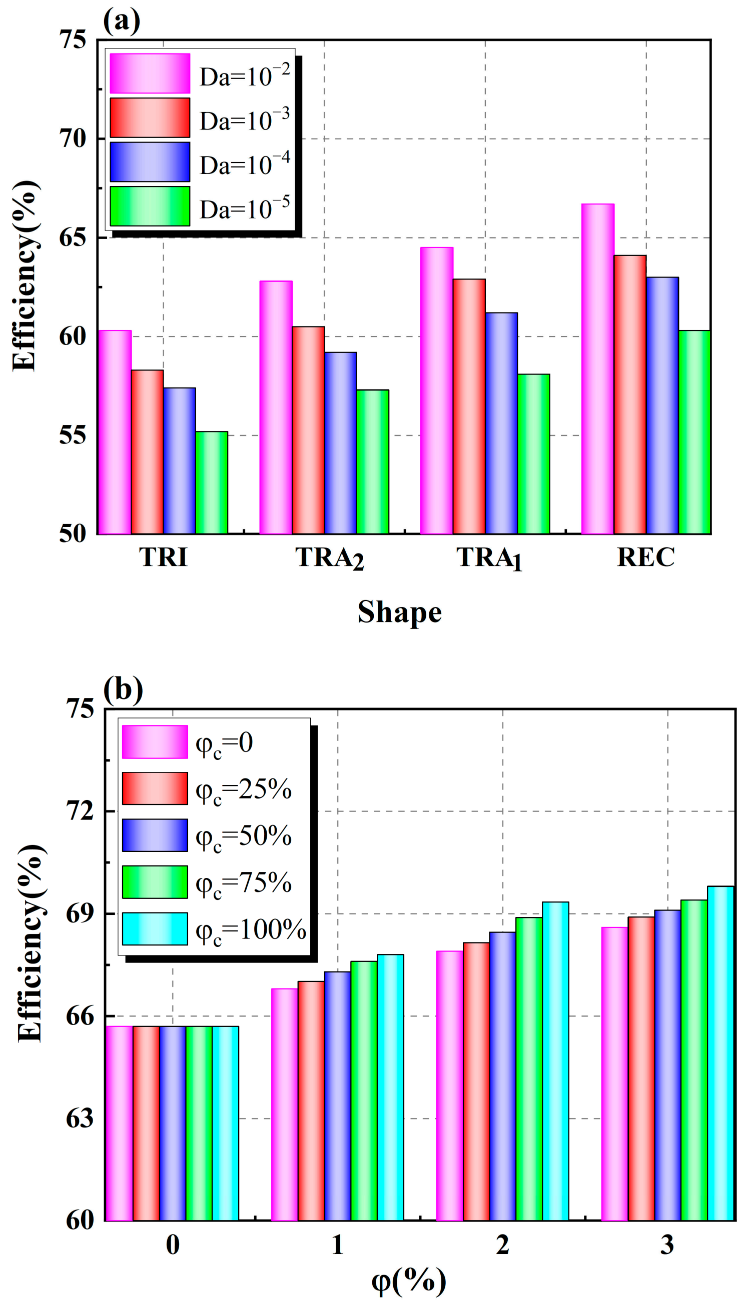

Figure 14. Thermal efficiency of FPSC channel at Re = 234: (**a**) the base fluid is water; (**b**) REC porous block $Da = 10^{-2}$.

4.4. Performance Evaluation Criteria (PEC)

Introducing porous blocks into the FPSC channel and substituting the base fluid with nanofluid significantly enhances heat transmission compared to the conventional

FPSC channel without inserts. However, this improvement comes at the cost of increased electricity consumption for pumping due to elevated pressure loss in the FPSC channel. Consequently, achieving a balance between pressure loss and enhanced heat transfer in the FPSC channel is crucial. To comprehensively assess the thermal performance of porous media and the enhancement of the FPSC channel facilitated by nanofluids, performance evaluation criteria (PEC) are employed [18]. The expression for PEC is outlined as follows:

$$\mathrm{PEC} = \frac{(Nu_{N=n}/Nu_{N=0})}{\left(\frac{f_{N=n}}{f_{N=0}}\right)^{1/3}} \tag{36}$$

Figure 15 depicts how the permeability and shape of the porous block, introduced in the base fluid condition, affect the performance evaluation criteria (PEC) of the FPSC channel. It is noteworthy that the shape has a substantial impact on the PEC, particularly under high Darcy number (Da = 10^{-2}, 10^{-3}) conditions. This is due to the observation that under conditions of elevated permeability, more fluid passes through the porous block, leading to a significantly enhanced effect of heat transfer area variation on the channel's heat transfer performance. Overall, it is evident that the peak thermal performance is observed at Da = 10^{-2} for REC shapes, establishing the FPSC channel as consistently demonstrating the highest PEC value. Specifically, as depicted in Figure 15a for the base fluid Re = 234, under conditions of low Darcy numbers (Da = 10^{-4}, 10^{-5}), the PEC value can achieve 1.68, the impact of porous block shape on the PEC value is not significant, and the PEC value persists below that of high Darcy number conditions (Da = 10^{-2}, 10^{-3}). This implies that irrespective of the shape of the porous block, the impact of pressure loss prevails in the FPSC channel at low Darcy number conditions, posing a hindrance to its objective of improving thermal performance. Additionally, under high Darcy number conditions (Da = 10^{-2}, 10^{-3}), for Reynolds numbers Re = 234 and 468, the PEC values consistently surpass 1.0. This signifies that the enhanced thermal performance of the FPSC channel outweighs the adverse impact of pressure loss. In conclusion, based on the synthesis of FPSC thermal performance evaluation, the configuration of the FPSC channel featuring an incorporated REC porous block, with a Darcy number of Da = 10^{-2} and Re = 234, exhibits the most effective heat transfer enhancement.

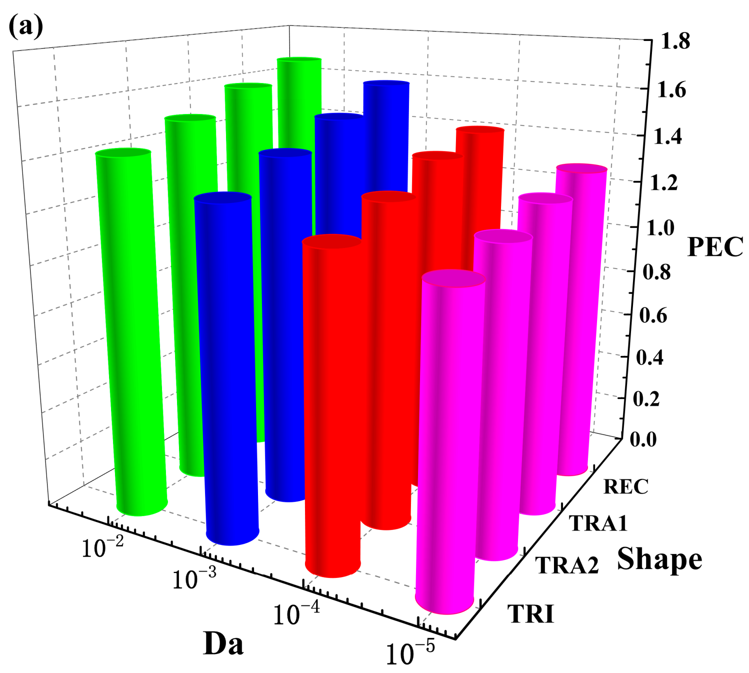

Figure 15. *Cont.*

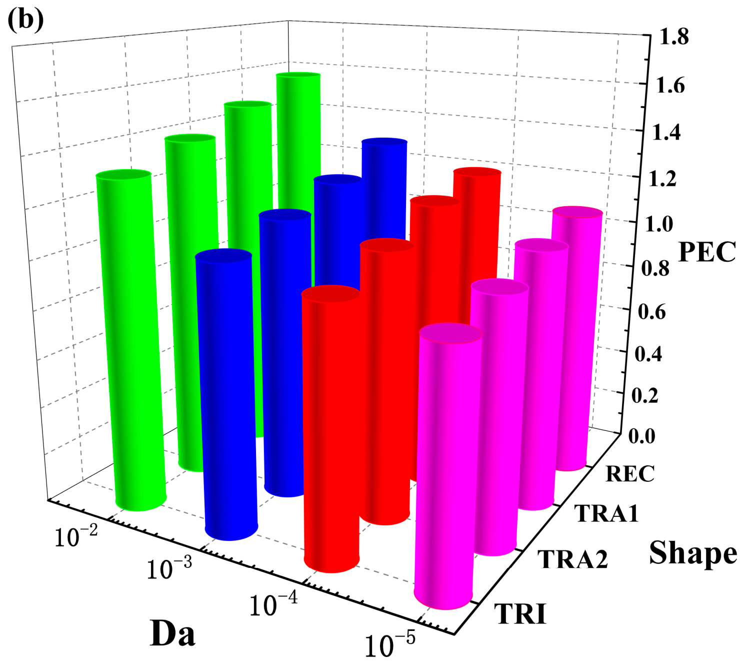

Figure 15. Variation of the performance evaluation criteria (PEC) in the FPSC channel with the shape change of inserted porous blocks at various *Da* and Reynolds numbers (*Re*): (**a**) *Re* = 234; (**b**) *Re* = 468.

Further, the intricate evolution of the PEC within the channel concerning the fluid Reynolds number parameter in response to the nanoparticle type, volume fraction, and Cu-Al_2O_3-H_2O mixing ratio is displayed in Figure 16. Calculations were conducted for the REC porous block with $Da = 10^{-2}$, revealing analytical results that indicate a noteworthy elevation in the PEC value of the channel upon the addition of nanoparticles in comparison to the base fluid. This holds true irrespective of the nanoparticle type, and the PEC value is positively correlated with the nanoparticle volume fraction, i.e., the larger the volume fraction, the larger the PEC, implying a better performance of the FPSC. In addition, we can find that at any nanoparticle volume fraction, the PEC increases as the percentage of Cu(φ_c) nanoparticles in Cu-Al_2O_3-H_2O increases. It is also worth mentioning that in condition φ_c = 0%, nanoparticles consist solely of Al_2O_3, and when the volume fraction is increased to φ_c = 100%, nanoparticles consist solely of Cu. Consequently, it is evident that Cu-H_2O can yield higher PEC values compared to Al_2O_3-H_2O. A comparison between Figure 16a and b distinctly indicates that the PEC value is higher at low Reynolds numbers (*Re* = 234) and decreases with increasing *Re*. Based on the analysis and comparison, it is concluded that under the conditions of REC porous block with $Da = 10^{-2}$ and *Re* = 234, when the nanoparticle volume fraction reaches 3%, along with the nanoparticle mixing ratio φ_c = 100%, the channel reaches its maximum PEC value of 1.9. This represents an enhancement in performance of approximately 90% compared to the empty channel.

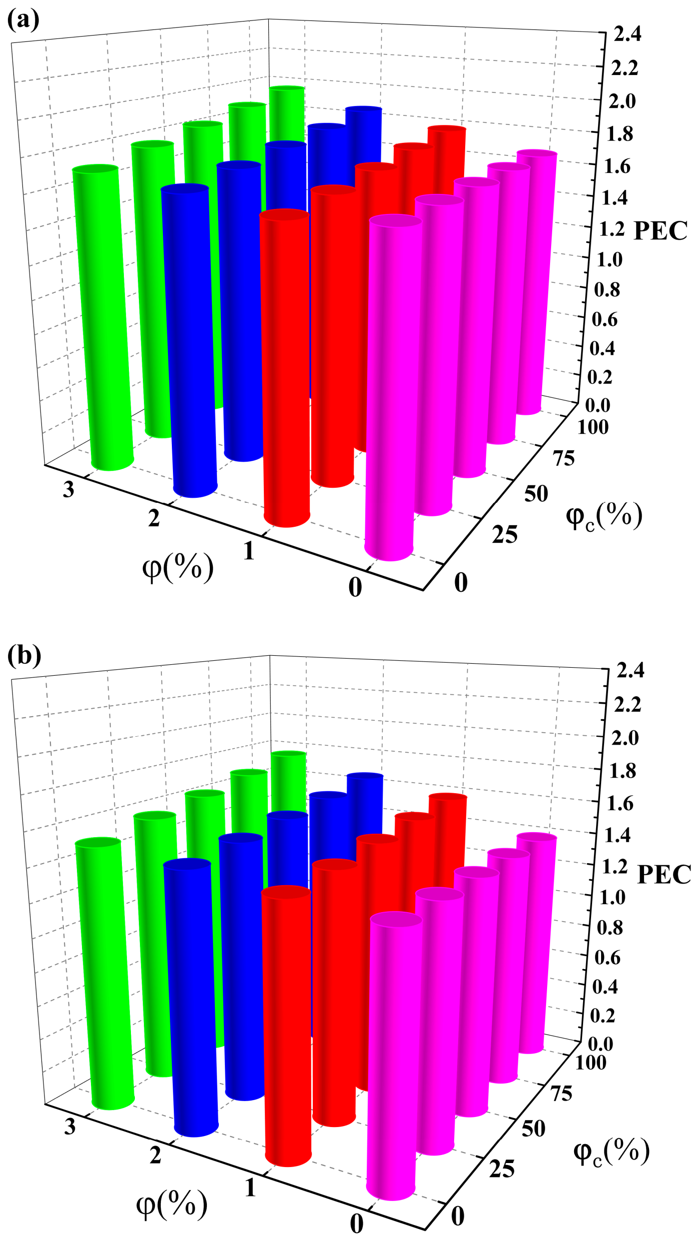

Figure 16. Variation of the performance evaluation criteria (PEC) versus the different volume fractions and mixing ratios of nanofluids for the cases of Reynolds numbers: (**a**) Re = 234; (**b**) Re = 468.

5. Conclusions

This study uses numerical modeling to examine how porous media and a flat-plate solar collector with nanofluid assistance can improve their thermal performance. Regarding the thermal efficiency of flat-plate solar collectors, the effects of porous blocks (considering both shape and permeability), as well as the influence of nanofluids (Reynolds number, type, volume fraction, mixing ratio), are thoroughly examined. Below is a summary of some of the findings' most important points.

(1) Regarding the impact of the flow state within the channel, observations indicate that fluids with high Reynolds numbers (within the laminar range) can markedly improve heat transfer performance within the FPSC channel. However, this improvement is counterbalanced by increased pumping power requirements. In scenarios with high Darcy numbers, the shape and permeability of the porous block demonstrate a substantial influence on heat transfer performance.

(2) The introduction of nanoparticles has a pronounced effect on the heat transfer performance within FPSC channels. It is apparent that a higher volume fraction of nanoparticles results in enhanced heat transfer performance. Additionally, the type of nanoparticles plays a critical role. Cu nanoparticles exhibit enhanced heat transfer performance compared to Al_2O_3 nanoparticles. Consequently, when both Al_2O_3 and Cu nanoparticles are introduced, a higher percentage of Cu nanoparticles results in improved heat transfer performance. Notably, the highest Nusselt number (Nu_g) achieved for the channel is 6.80, achieved with a nanoparticle volume fraction of 3% and φ_c = 100%.
(3) Additional analysis of the thermal efficiency in the FPSC channel reveals that at Re = 234, the thermal efficiency is high and is notably affected by the shape of the porous block, with superior performance observed in the REC porous block configuration and the large Da values. For instance, when the volume percentage of nanoparticles is 3% and φ_c = 100%, the thermal efficiency can reach a maximum of 70.5%, which is roughly 2.5% greater than that of φ_c = 0% (the nanoparticle is Al_2O_3).
(4) A comprehensive performance evaluation criteria (PEC) analysis for FPSC indicates that the rectangular REC porous block configuration performs optimally for high Darcy numbers ($Da = 10^{-2}$). Taking into account the influence of the flow regime in the FPSC channel, the PEC value reaches its peak at 1.68 under conditions of low Reynolds numbers (Re = 234), representing a 68% enhancement compared to an empty channel. Furthermore, it is crucial to emphasize that the PEC is affected by the characteristics of the heat transfer fluid, with a maximum value of 1.90 attained for the channel PEC under the condition of a nanoparticle volume fraction of 3% and φ_c = 100%.

Author Contributions: X.L. (Xinwei Lin): Methodology, Software, Validation, Investigation, Writing—Original Draft, and Visualization. Y.X.: Software, Validation, Investigation, Writing—Review Editing, Project Administration, and Funding Acquisition. Z.C.: Conceptualization, Formal analysis, Data Curation, and Supervision. X.L. (Xianshuang Liu): Software, Formal Analysis, and Resources. Y.F.: Software, Formal Analysis, and Resources. L.L.: Software and Formal Analysis. W.Z.: Formal Analysis and Resources. All authors have read and agreed to the published version of the manuscript.

Funding: This research was funded by the National Natural Science Foundation of China (Grant No. 51406123), the University Synergy Innovation Program of Anhui Province (Grant No. GXXT-2022-017), and the Key Project of Anhui Provincial University Research and Development (CN) (Grant No. 2023AH050188).

Informed Consent Statement: Informed consent was obtained from all subjects involved in the study.

Data Availability Statement: Data are contained within the article.

Acknowledgments: The authors would like to extend their sincere appreciation to the support from the National Natural Science Foundation of China, the University Synergy Innovation Program of Anhui Province, and the Key Project of Anhui Provincial University Research and Development (CN).

Conflicts of Interest: The authors declare no conflicts of interest.

References

1. Said, Z.; Hachicha, A.A.; Aberoumand, S.; Yousef, B.A.A.; Sayed, E.T.; Bellos, E. Recent advances on nanofluids for low to medium temperature solar collectors: Energy, exergy, economic analysis and environmental impact. *Prog. Energy Combust. Sci.* **2021**, *84*, 100898. [CrossRef]
2. Hashim, W.M.; Shomran, A.T.; Jurmut, H.A.; Gaaz, T.S.; Kadhum, A.A.H.; Al-Amiery, A.A. Case study on solar water heating for flat plate collector. *Case Stud. Therm. Eng.* **2018**, *12*, 666–671. [CrossRef]
3. Sakhaei, S.A.; Valipour, M.S. Performance enhancement analysis of The flat plate collectors: A comprehensive review. *Renew. Sustain. Energy Rev.* **2019**, *102*, 186–204. [CrossRef]
4. Wang, D.; Mo, Z.; Liu, Y.; Ren, Y.; Fan, J. Thermal performance analysis of large-scale flat plate solar collectors and regional applicability in China. *Energy* **2022**, *238*, 121931. [CrossRef]

5. Vengadesan, E.; Senthil, R. Experimental thermal performance and enviroeconomic analysis of serpentine flow channeled flat plate solar water collector. *Environ. Sci. Pollut. Res. Int.* **2022**, *29*, 17241–17259. [CrossRef] [PubMed]
6. Bhattacharyya, S.; B, H.; Paul, A. The effect of circular hole spring tape on the turbulent heat transfer and entropy analysis in a heat exchanger tube: An experimental study. *Exp. Heat Transf.* **2020**, *34*, 493–512. [CrossRef]
7. Garcia, R.P.; Oliveira, S.d.R.; Scalon, V.L. Thermal efficiency experimental evaluation of solar flat plate collectors when introducing convective barriers. *Sol. Energy* **2019**, *182*, 278–285. [CrossRef]
8. Aref, L.; Fallahzadeh, R.; Shabanian, S.R.; Hosseinzadeh, M. A novel dual-diameter closed-loop pulsating heat pipe for a flat plate solar collector. *Energy* **2021**, *230*, 120751. [CrossRef]
9. Chen, C.-C.; Huang, P.-C.; Hwang, H.-Y. Enhanced forced convective cooling of heat sources by metal-foam porous layers. *Int. J. Heat Mass Transf.* **2013**, *58*, 356–373. [CrossRef]
10. Ahmadi, A.; Ehyaei, M.A.; Doustgani, A.; El Haj Assad, M.; Hmida, A.; Jamali, D.H.; Kumar, R.; Li, Z.X.; Razmjoo, A. Recent residential applications of low-temperature solar collector. *J. Clean. Prod.* **2021**, *279*, 123549. [CrossRef]
11. Gorjian, S.; Ebadi, H.; Calise, F.; Shukla, A.; Ingrao, C. A review on recent advancements in performance enhancement techniques for low-temperature solar collectors. *Energy Convers. Manag.* **2020**, *222*, 113246. [CrossRef]
12. Tonekaboni, N.; Salarian, H.; Nimvar, M.E.; Khaleghinia, J. Exergoeconomic analysis of a solar CCHP with partially porous material filled collector. *Int. J. Exergy* **2022**, *37*, 181–199. [CrossRef]
13. Alagumalai, A.; Qin, C.; Vimal, K.E.K.; Solomin, E.; Yang, L.; Zhang, P.; Otanicar, T.; Kasaeian, A.; Chamkha, A.J.; Rashidi, M.M.; et al. Conceptual analysis framework development to understand barriers of nanofluid commercialization. *Nano Energy* **2022**, *92*, 106736. [CrossRef]
14. Menni, Y.; Chamkha, A.J.; Azzi, A. Nanofluid flow in complex geometries a review. *J. Nanofluids* **2019**, *8*, 893–916. [CrossRef]
15. Zaboli, M.; Saedodin, S.; Ajarostaghi, S.S.M.; Karimi, N. Recent progress on flat plate solar collectors equipped with nanofluid and turbulator: State of the art. *Environ. Sci. Pollut. Res. Int.* **2023**, *30*, 109921–109954. [CrossRef]
16. Jouybari, H.J.; Saedodin, S.; Zamzamian, A.; Nimvari, M.E. Experimental investigation of thermal performance and entropy generation of a flat-plate solar collector filled with porous media. *Appl. Therm. Eng.* **2017**, *127*, 1506–1517. [CrossRef]
17. Ali, R.M.K.; Lafta Ghashim, S. Numerical analysis of the heat transfer enhancement by using metal foam. *Case Stud. Therm. Eng.* **2023**, *49*, 103336. [CrossRef]
18. Anirudh, K.; Dhinakaran, S. Numerical analysis of the performance improvement of a flat-plate solar collector using conjugated porous blocks. *Renew. Energy* **2021**, *172*, 382–391. [CrossRef]
19. Fu, Y.; Xia, Y.; Lin, X.; Cheng, Z.; Zhang, Z.; Feng, J.; Wang, H. A novel structure design and numerical analysis of porous media-assisted enhanced thermal performance of flat-plate solar collector. *Therm. Sci. Eng. Prog.* **2023**, *40*, 101777. [CrossRef]
20. Bovand, M.; Rashidi, S.; Esfahani, J.A. Heat transfer enhancement and pressure drop penalty in porous solar heaters: Numerical simulations. *Sol. Energy* **2016**, *123*, 145–159. [CrossRef]
21. Saedodin, S.; Zamzamian, S.A.H.; Nimvari, M.E.; Wongwises, S.; Jouybari, H.J. Performance evaluation of a flat-plate solar collector filled with porous metal foam: Experimental and numerical analysis. *Energy Convers. Manag.* **2017**, *153*, 278–287. [CrossRef]
22. Anirudh, K.; Dhinakaran, S. Performance improvement of a flat-plate solar collector by inserting intermittent porous blocks. *Renew. Energy* **2020**, *145*, 428–441. [CrossRef]
23. Xia, Y.; Lin, X.; Shu, Y.; Cheng, Z. Enhanced thermal performance of a flat-plate solar collector inserted with porous media: A numerical simulation study. *Therm. Sci. Eng. Prog.* **2023**, *44*, 102063. [CrossRef]
24. Ziyadanogullari, N.B.; Yucel, H.L.; Yildiz, C. Thermal performance enhancement of flat-plate solar collectors by means of three different nanofluids. *Therm. Sci. Eng. Prog.* **2018**, *8*, 55–65. [CrossRef]
25. Saffarian, M.R.; Moravej, M.; Doranehgard, M.H. Heat transfer enhancement in a flat plate solar collector with different flow path shapes using nanofluid. *Renew. Energy* **2020**, *146*, 2316–2329. [CrossRef]
26. Gupta, S.; Rajale, S.; Raval, F.; Sojitra, M.; Tiwari, A.K.; Joshi, A.; Singh, R. Comparative performance analysis of flat plate solar collectors with and without aluminium oxide-based nano-fluid. *Mater. Today Proc.* **2021**, *46*, 5378–5383. [CrossRef]
27. Darbari, B.; Rashidi, S. Thermal efficiency of flat plate thermosyphon solar water heater with nanofluids. *J. Taiwan Inst. Chem. Eng.* **2021**, *128*, 276–287. [CrossRef]
28. Esmaeili, M.; Karami, M.; Delfani, S. Performance enhancement of a direct absorption solar collector using copper oxide porous foam and nanofluid. *Int. J. Energy Res.* **2020**, *44*, 5527–5544. [CrossRef]
29. Xiong, Q.; Tayebi, T.; Izadi, M.; Siddiqui, A.A.; Ambreen, T.; Li, L.K.B. Numerical analysis of porous flat plate solar collector under thermal radiation and hybrid nanoparticles using two-phase model. *Sustain. Energy Technol. Assess.* **2021**, *47*, 101404. [CrossRef]
30. NematpourKeshteli, A.; Iasiello, M.; Langella, G.; Bianco, N. Increasing melting and solidification performances of a phase change material-based flat plate solar collector equipped with metal foams, nanoparticles, and wavy wall-Y-shaped surface. *Energy Convers. Manag.* **2023**, *291*, 117–268. [CrossRef]
31. Aghili Yegane, S.P.; Kasaeian, A. Thermal performance assessment of a flat-plate solar collector considering porous media, hybrid nanofluid and magnetic field effects. *J. Therm. Anal. Calorim.* **2020**, *141*, 1969–1980. [CrossRef]
32. Vafai, K.; Tien, C.L. Boundary and inertia effects on flow and heat transfer in porous media. *Int. J. Heat Mass Transf.* **1981**, *24*, 195–203. [CrossRef]
33. Vijaybabu, T.R.; Anirudh, K.; Dhinakaran, S. LBM simulation of unsteady flow and heat transfer from a diamond-shaped porous cylinder. *Int. J. Heat Mass Transf.* **2018**, *120*, 267–283. [CrossRef]

34. Chen, Z.; Gu, M.; Peng, D. Heat transfer performance analysis of a solar flat-plate collector with an integrated metal foam porous structure filled with paraffin. *Appl. Therm. Eng.* **2010**, *30*, 1967–1973. [CrossRef]
35. Samiezadeh, S.; Khodaverdian, R.; Doranehgard, M.H.; Chehrmonavari, H.; Xiong, Q. CFD simulation of thermal performance of hybrid oil-Cu-Al_2O_3 nanofluid flowing through the porous receiver tube inside a finned parabolic trough solar collector. *Sustain. Energy Technol. Assess.* **2022**, *50*, 101888. [CrossRef]
36. Zhou, S.-Q.; Ni, R. Measurement of the specific heat capacity of water-based Al_2O_3 nanofluid. *Appl. Phys. Lett.* **2008**, *92*, 093123. [CrossRef]
37. Jouybari, H.J.; Saedodin, S.; Zamzaman, A.; Nimvari, M.E.; Wongwises, S. Effects of porous material and nanoparticles on the thermal performance of a flat plate solar collector: An experimental study. *Renew. Energy* **2017**, *114*, 1407–1418. [CrossRef]